

# Unexpected Consequences of Transverse Isotropy

Hitoshi Kawakatsu<sup>\*1</sup>

## ABSTRACT

In a series of articles, [Kawakatsu et al. \(2015\)](#) and [Kawakatsu \(2016a,b, 2018\)](#) introduced and discussed a new parameter,  $\eta_{\kappa}$ , that characterizes the incidence angle dependence (relative to the symmetry axis) of seismic body-wave velocities in a transverse isotropy (TI) system. During the course of these exercises, several nontrivial consequences of TI were realized and summarized as follows: (1) *P*-wave velocity (anisotropy) strongly influences the conversion efficiency of *P*-to-*S* and *S*-to-*P*, as much as *S*-wave velocity perturbation does; (2) Rayleigh-wave phase velocity has substantial sensitivity to *P*-wave anisotropy near the surface; (3) a trade-off exists between  $\eta_{\kappa}$  and the  $V_p/V_s$  ratio if the latter is sought under an assumption of isotropy or the elliptic condition. Among these findings, the first two deserve careful attention in interpretation of results of popular seismic analysis methods, such as receiver function analysis and ambient-noise Rayleigh-wave dispersion analysis. We present simple example cases for such problems to delineate the effect in actual situations, as well as scalings among TI parameters of the crust and mantle materials or models that might help understanding to what extent the effect becomes important.

## KEY POINTS

- We present consequences of transverse isotropy deserving attention in popular seismic analysis methods.
- *P*-wave anisotropy greatly influences the receiver function and Rayleigh-wave dispersion.
- We need to be careful to interpret the results of such popular analysis methods when anisotropy is present.

[Supplemental Material](#)

## INTRODUCTION

[Kawakatsu \(2018\)](#) recently showed that reflection and transmission of plane waves in a transversely isotropic system with a vertical symmetry axis (VTI) had unexpected properties by the analogy of the corresponding isotropic case: *P* wavespeed (anisotropy) strongly influences the conversion efficiency of *P*-to-*S* and *S*-to-*P*, as much as *S* wavespeed perturbation does. It was also pointed out that, with the properly defined set of VTI parameters using the new fifth parameter,  $\eta_{\kappa}$ , Rayleigh-wave phase velocity had substantial increased sensitivity to the shallowmost *P*-wave anisotropy, especially near the surface, although the sensitivity is generally much reduced elsewhere. This suggests that *P*-wave anisotropy might have significant consequences for the interpretation of receiver functions and/or ambient-noise Rayleigh-wave dispersion measurements that are now commonly employed in crustal and mantle studies of shear velocity. The purpose of this short note is to present such example case waveforms for receiver function analysis

and Rayleigh-wave sensitivity kernels for 1D VTI structures to draw the attention of researchers in the related fields.

## REPRESENTATION OF VTI OR RADIAL ANISOTROPY

In a VTI, or equivalently radial anisotropy, system, horizontally and vertically propagating *P*-waves have phase velocities of

$$\alpha_H = \sqrt{A/\rho}, \quad (1)$$

and

$$\alpha_V = \sqrt{C/\rho}, \quad (2)$$

respectively, in which  $\rho$  gives the density. As for shear waves, horizontally and vertically polarized horizontally propagating *S* waves, respectively, have phase velocities of

$$\beta_H = \sqrt{N/\rho}, \quad (3)$$

and

$$\beta_V = \sqrt{L/\rho}, \quad (4)$$

and vertically propagating *S* waves also have a phase velocity of  $\beta_V$  (e.g., see fig. 1 of [Kawakatsu, 2016a](#)). So, for these horizontally

1. Earthquake Research Institute, The University of Tokyo, Bunkyo-ku, Tokyo, Japan

\*Corresponding author: hitosi@eri.u-tokyo.ac.jp

**Cite this article as** Kawakatsu, H. (2020). Unexpected Consequences of Transverse Isotropy, *Bull. Seismol. Soc. Am.* **111**, 129–138, doi: [10.1785/B0120200205](https://doi.org/10.1785/B0120200205)

© Seismological Society of America

or vertically traveling body waves, phase velocities are given by the four elastic constants,  $A$ ,  $C$ ,  $L$  and  $N$ , and the ratios of these elastic constants define the degree of radial anisotropy,

$$\varphi^{-1} = A/C = \alpha_H^2/\alpha_V^2, \quad (5)$$

for the  $P$  wave, and

$$\xi = N/L = \beta_H^2/\beta_V^2, \quad (6)$$

for the  $S$  wave (Takeuchi and Saito, 1972). As for the  $P$ -wave anisotropy index, we specifically use  $\varphi^{-1}$  because, for many of realistic cases, the strength of anisotropy for  $P$  and  $S$  is positively correlated and having  $\alpha_V$  as a reference (i.e., denominator) is more reasonable for a layered VTI medium as in Thomsen's parameters (Thomsen, 1986). For other intermediate direction body waves, the fifth elastic constant,  $F$ , affects the incidence angle dependence of quasi- $P$  and quasi- $SV$  waves via  $\eta_\kappa$  (Kawakatsu, 2016a):

$$\eta_\kappa = \frac{(F + L)}{(A - L)^{1/2}(C - L)^{1/2}}. \quad (7)$$

### SYNTHETIC WAVEFORM EXAMPLES: $P_s$ OR $Sp$ CONVERSION WITHOUT $S$ WAVESPEED PERTURBATION

We consider the elastic response (noise free) of a homogeneous layer (80 km thick) over a homogeneous half-space to incident  $P$  or  $S$  plane waves. As for a reference isotropic case, the upper layer is given by a Poisson solid with  $P$ -wave and  $S$ -wave velocities and density given by  $\alpha_1 = 8.0$  km/s,  $\beta_1 = 4.6188$  km/s, and  $\rho_1 = 3.3$  g/cc and the lower half-space with 5% velocity reduction for  $S$  but not for  $P$  and density. As for anisotropic cases, for the sake of simplicity, we introduce anisotropy only for the lower layer. We employ anisotropy strength,  $a_p$  and  $a_s$ , to specify anisotropic velocities as

$$\alpha_{H/V} = \alpha_0(1 \mp a_p/2), \quad \beta_{H/V} = \beta_0(1 \mp a_s/2),$$

in which  $\alpha_0 = (\alpha_V + \alpha_H)/2$  and  $\beta_0 = (\beta_V + \beta_H)/2$  denote reference isotropic wavespeeds, and  $a_p = (\alpha_V - \alpha_H)/\alpha_0$ ,  $a_s = (\beta_V - \beta_H)/\beta_0$ . Also, for the sake of simplicity, we assume the elliptic condition (i.e.,  $\eta_\kappa = 1.0$ ) in which a phase slowness surface of  $P$  wave becomes elliptic (Kawakatsu, 2016a). It should be also noted that  $S$ -wave anisotropy itself does not directly enter in the  $P/SV$  coupling in VTI, and thus the effect of changing it is equivalent to that of changing the  $S$  wavespeed,  $\beta_V$ .

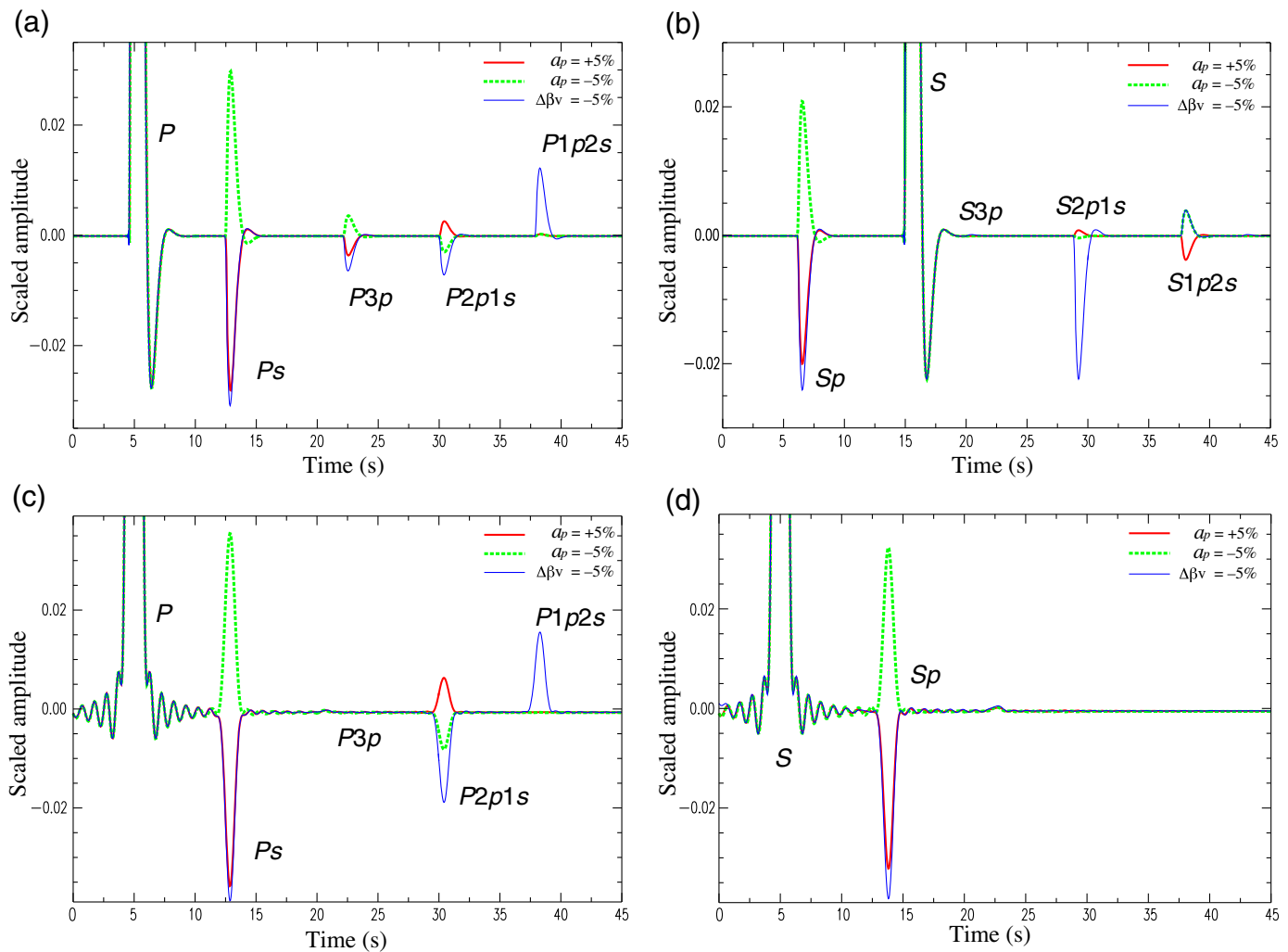
In Figure 1a, instead of receiver functions, we show radial-component waveforms at a surface point of the top layer; as for the waveform for the primary  $P$ - $S$  conversion phase, the isotropic case (thin line) with 5%  $S$ -speed reduction is almost identical to the anisotropic case with  $a_p = 5\%$  (thick line), whereas one with  $a_p = -5\%$  (broken line) exhibits reversed polarity. For

anisotropic cases, the situation is consistent with the properties of the transmission coefficients described in Kawakatsu (2018). An  $S$  wavespeed reduction of 5% generates a converted phase nearly equivalent to that caused by  $P$ -wave anisotropy of  $a_p = 5\%$ , which makes  $\alpha_V$  ( $\alpha_H$ ) 2.5% faster (slower) than the reference velocity,  $\alpha_0$ . For the secondary multiples, the situation is different, indicating a possibility of differentiating the effects of  $S$  wavespeed and  $P$ -wave anisotropy. A similar observation can be made for the case of the  $S$ -wave incidence; in Figure 1b, the vertical component of  $S$ -wave waveforms that is used for  $S$ -receiver function is shown. The precursors to  $S$ , that is,  $Sp$ , show similar behavior to  $Ps$  for the  $P$ -wave case; that is, the significant effect of  $P$  anisotropy on  $S$ -to- $P$  conversion can be seen. It should be noted that the amplitudes in Figure 1 depend on the slowness of incoming plane waves and will vary differently with the ray parameter depending on the arrival type (primary conversions vs. multiples, etc.). The ray parameter of 0.06 s/km employed for the synthetic waveforms presented in Figure 1a,c is a typical one for the teleseismic  $P$ -wave case (0.04–0.08 s/km). The ray parameter of 0.09 s/km for the  $S$ -wave incidence case (Fig. 1b,d) corresponds to the lower end of the teleseismic range (0.09–0.12 s/km). Although the amplitudes of the primary conversion phases ( $Ps$  and  $Sp$ ), which are the main focus of this article, vary depending on the employed ray parameter within the teleseismic range, the significant effect of  $P$  anisotropy compared with that of the  $S$  wavespeed reduction discussed earlier is unchanged.

### SIGNIFICANCE OF $P$ -WAVE ANISOTROPY IN RECEIVER FUNCTION ANALYSIS

It is well known for isotropic material that  $P$ -to- $S$  and  $S$ -to- $P$  conversions have a strong sensitivity to  $S$  wavespeed perturbation and a weak one to density (note however that multiples have a higher sensitivity to density contrasts), but no sensitivity to  $P$  wavespeed in the first order (e.g., Aki and Richards, 1980). Based on this, in most receiver function analyses, we generally assume the primary converted phases to represent the structure of the  $S$  wavespeed perturbation. Kawakatsu (2018), on the other hand, showed that once anisotropy (transverse isotropy [TI]) was considered,  $P$ -wave anisotropy was as important as  $S$ -wave structure, and in this article, we present simple 1D examples of converted waveforms without  $S$ -wave perturbations (Fig. 1).

Figure 1 indicates that  $P$  anisotropy of +5% ( $a_p = 0.05$ ) gives comparable amplitude of  $Ps$  (or  $Sp$ ) phase to  $S$  wavespeed reduction of 5% ( $\Delta\beta_V = -5\%$ ). Radial anisotropy on the order of 5% or larger has been reported for the oceanic crust (Russell et al., 2019) and the mantle (asthenosphere) (e.g., Nettles and Dziewonski, 2008) and 10% ~ 30% beneath active volcanoes (Jaxybulatov et al., 2014; Nagaoka, 2020). To examine a more realistic situation, let us consider a case of fabrics representing the mantle. It is generally known that  $P$  and  $S$  anisotropy correlates positively for mantle fabrics (e.g., Montagner and Anderson, 1989; Becker et al., 2006). Consider a case that the



strength of  $P$ - and  $S$ -wave anisotropy is comparable (i.e.,  $a_p \sim a_s$ ,  $\phi^{-1} \sim \xi$ ); then  $P$  anisotropy of  $-5\%$  means  $S$  anisotropy of  $-5\%$ , equivalent to  $\Delta\beta_V = -2.5\%$  in the case of Figure 1. Therefore, the contributions of  $P$  and  $S$  anisotropy to the  $P_s$  phase are opposite in sign, and the  $P$ -anisotropy contribution dominates. This is somewhat paradoxical, but it is the case: that is, when  $\beta_V$  decreases, the corresponding receiver function shows a positive primary  $P_s$  phase if it is due solely to the fabric. Thus, in environments where seismic anisotropy is important, the interpretation of receiver functions may require careful attention (e.g., lithosphere–asthenosphere boundary [LAB], mid-lithospheric discontinuity [MLD], or Moho; Kawakatsu *et al.*, 2009; Abt *et al.*, 2010; Brownlee *et al.*, 2017, respectively).

### RAYLEIGH-WAVE SENSITIVITY TO NEAR-SURFACE $P$ ANISOTROPY

A small change in the phase velocity ( $c$ ) of surface waves at a given angular frequency ( $\omega$ ) due to changes in material properties is expressed as

$$\left(\frac{\delta c}{c}\right)_\omega = \sum_i \int K_{\epsilon_i}(z) \left(\frac{\delta \epsilon_i}{\epsilon_i}\right) dz, \quad (8)$$

**Figure 1.** Synthetic elastic responses at the surface of a homogeneous isotropic layer over a homogeneous VTI half-space: (a) the radial component of a plane  $P$ -wave incidence case (ray parameter: 0.06 s/km); (b) the vertical component of a plane  $S$ -wave incidence case (0.09 s/km). Three cases for the half-space are shown for  $a_p = +5\%$  (solid line),  $a_p = -5\%$  (thick broken line), and isotropic with  $\beta_V$  reduction of 5% (thin solid line). The amplitude is scaled with that of the main phase (i.e., (a)  $P$  vertical and (b)  $S$  radial) and multiplied by  $-1$  for (b) the  $S$ -wave case, and a low-pass (2s) causal Butterworth filter is applied. For multiple phases, the number of  $P$  and/or  $S$  legs in the upper layer are indicated. These waveforms provide essential information for receiver functions (e.g., Ammon, 1991), but corresponding receiver functions are also shown for (c)  $P$ -receiver functions and for (d)  $S$ -receiver functions; they are calculated via the spectral domain deconvolution with a water level of 0.01 and the Gaussian filter coefficient  $a = 2.0$ ; no L-Q coordinate rotation is applied. For  $S$ -receiver function, time is reversed and the amplitude is multiplied by  $-1$  so that both receiver functions show similar primary  $P_s$ - and  $Sp$ -phase appearance. Synthetic seismograms are calculated with a locally developed Haskell matrix code for VTI. The color version of this figure is available only in the electronic edition.

in which  $\epsilon_i$  denotes the  $i$ th elastic parameter among five anisotropy parameters of VTI or the density at a depth  $z$  and  $K_{\epsilon_i} = \frac{\epsilon_i}{c} \left[ \frac{\partial c}{\partial \epsilon_i} \right]_\omega$  represents the corresponding sensitivity kernel

(partial derivative) (e.g., Takeuchi and Saito, 1972; Aki and Richards, 1980). For Rayleigh waves, when we use the set  $(\alpha_H, \alpha_V, \beta_H, \beta_V, \eta_\kappa)$  or  $\eta$  as parameters, in which  $\eta = F/(A - 2L)$  is the conventional fifth parameter defined by Takeuchi and Saito (1972), the explicit expressions for  $K_{\varepsilon_i}$ 's are given in Kawakatsu (2016b). The influence of  $P$ -anisotropy change on  $c$  is written as

$$\begin{aligned} \left(\frac{\delta c}{c}\right)_\omega &= \int \left\{ K_{\alpha_V}(z) \left(\frac{\delta \alpha_V}{\alpha_V}\right) + K_{\alpha_H}(z) \left(\frac{\delta \alpha_H}{\alpha_H}\right) \right\} dz \\ &= \int \left\{ (K_{\alpha_V} + K_{\alpha_H}) \left(\frac{\delta \alpha_0}{\alpha_0}\right) + \left(\frac{K_{\alpha_V} - K_{\alpha_H}}{2}\right) \delta a_p \right\} dz, \end{aligned} \quad (9)$$

assuming the initial unperturbed state is isotropic, that is,  $\alpha_V = \alpha_H = \alpha_0$ .

Kawakatsu (2016b) pointed out that, with the introduction of the properly defined set of VTI parameters with  $\eta_\kappa$ , the Rayleigh-wave sensitivity kernel to  $P$  anisotropy was significantly modified and some of the previously claimed sensitivity (Dziewonski and Anderson, 1981; Anderson and Dziewonski, 1982) was an inappropriate projection of the sensitivity of  $S$  anisotropy into that of  $P$  anisotropy. Figure 2 shows such Rayleigh-wave sensitivity kernels with the new parameters using equation (9) at the peak period of the microseisms (7 s), which are now commonly used to infer the subsurface structure via ambient-noise dispersion analysis (e.g., Shapiro and Campillo, 2004; Nishida *et al.*, 2008). The  $P$ -anisotropy kernel ( $a_p$ ) shows a sharp increase in sensitivity (i.e., the absolute amplitude) near the surface (from nearly zero at a depth of 2.5 km to  $|-0.08|$  at 0 km), although the amplitude is generally reduced elsewhere. For the top 2 km, the sensitivity to  $a_p$  is as large as that to  $\beta_V$ . Considering that  $\delta\beta_V \sim a_s/2$ , this indicates that the sensitivity to  $P$  anisotropy is nearly twice as large as that to  $S$  anisotropy and the sign is opposite; this characteristic is quite similar to that of  $P$ - $S$  and  $S$ - $P$  conversions discussed earlier and appears to indicate that the increase of  $P$ -anisotropy sensitivity near the surface is related to  $P$ - $S$  and  $S$ - $P$  conversions at the free surface.

This may affect the interpretation of ambient-noise tomography (e.g., Lin *et al.*, 2010), as well as time-lapse measurements of phase velocity (e.g., Brenguier, Campillo, *et al.*, 2008; Brenguier, Shapiro, *et al.*, 2008; Nishida *et al.*, 2020). For example, introducing  $P$  anisotropy of  $a_p = 5\%$  (while keeping  $\beta_V$  and  $\eta_\kappa$  constant, but not  $\eta$ , which is essential; Kawakatsu, 2016b) for the top 2.25 km of the model in Figure 2 (i.e., flat preliminary reference Earth model [PREM], Dziewonski and Anderson, 1981 without water layer) will decrease the phase velocity by about 0.37%. This value is about one order of magnitude larger than those observed in pre-eruption phases at the Piton de la Fournaise volcano (Brenguier, Shapiro, *et al.*, 2008) and Shinmoe-dake of the Kirishima volcano (Nishida *et al.*, 2020), and postseismically in Parkfield (Brenguier, Campillo, *et al.*, 2008); that is, a change of near-surface  $P$  anisotropy of  $a_p \sim 0.5\%$  that might be caused

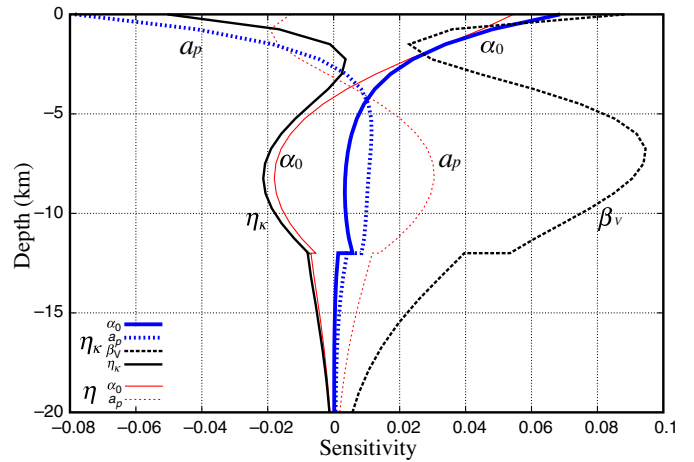


**Figure 2.** Partial derivatives (sensitivity kernels) for fundamental mode Rayleigh wave at a period of 7 s calculated for a flat preliminary reference Earth model (PREM) without the water layer. The figure compares the anisotropic  $P$ -wave sensitivity for  $(\alpha_H, \alpha_V, \beta_H, \beta_V, \eta_\kappa)$  or  $\eta$  parameter sets, in which  $\eta = F/(A - 2L)$  is the conventional fifth parameter defined by Takeuchi and Saito (1972). Note that  $P$ -wave sensitivity is generally reduced for the  $\eta_\kappa$  case (thick solid and dotted lines) compared with the conventional  $\eta$  case (thin solid and dotted lines), but it is increased near the surface. For details, see the [Rayleigh-Wave Sensitivity to Near-Surface  \$P\$  Anisotropy](#) section and Kawakatsu (2016b). The color version of this figure is available only in the electronic edition.

by, for example, opening or healing of cracks (e.g., Crampin, 1984), could potentially explain those observations. Figure 2 indicates that the sensitivities of the Rayleigh-wave phase velocity to near-surface  $a_p$  and  $a_s$  ( $\beta_V$ ) are opposite in sign; that is, if  $P$  and  $S$  anisotropy are positively correlated, the near-surface net effect tends to cancel each other depending on the degree of the correlation; if they are linearly correlated as discussed for the case of  $P$ - $S$  conversion before, the effect of  $P$  anisotropy dominates the phase velocity change. Therefore, if anisotropy becomes an important factor, the interpretation might not be straightforward.

### TRADE-OFF BETWEEN $\eta_\kappa$ AND $V_p/V_s$ RATIO

The incidence angle dependence of quasi- $P$ - and  $SV$ -wave phase velocities on  $\eta_\kappa$  indicates that the effect is opposite between  $P$  and  $SV$ ; that is, in the propagation direction in which  $P$  velocity increases,  $SV$  velocity decreases and vice versa (Fig. 3). This suggests that if this effect is ignored (i.e., if the elliptic condition or isotropy is assumed), the estimate of the  $V_p/V_s$  ratio can be biased. The spherical average of this effect can be estimated under the assumption of weak anisotropy as

$$\frac{\overline{V_p}}{\overline{V_{SV}}} \approx \frac{\alpha_V}{\beta_V} \left(1 - \frac{8}{45} \sigma\right) \approx \frac{\alpha_V}{\beta_V} \left[1 + \frac{16}{45} (\eta_\kappa - 1)\right], \quad (10)$$

in which, using Thomsen parameters, the following approximation is employed,

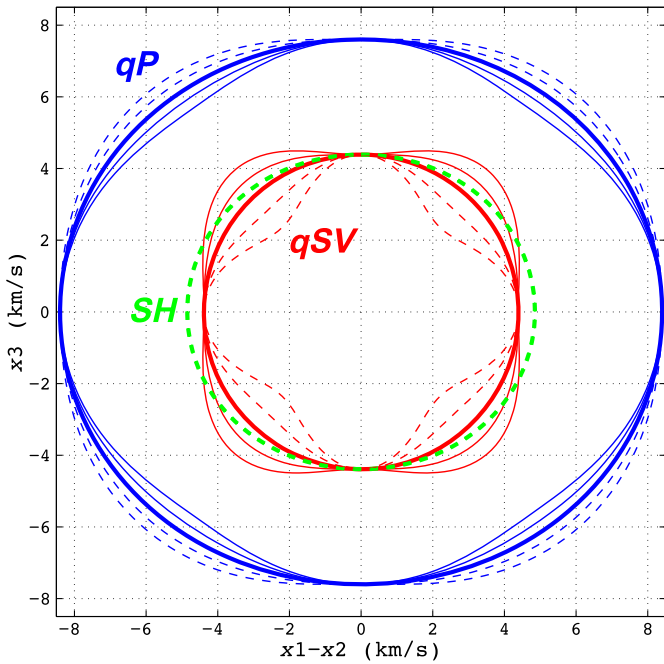


**Figure 3.** Phase velocity surfaces of body waves for five VTI models that have common  $P$ - and  $S$ -wave anisotropy ( $a_p = a_s = -0.1$ ): outer set of five lines for quasi- $P$  wave, inner set of five lines for quasi- $SV$  wave, and thick broken ellipse for  $SH$  wave. Thick solid lines show cases in which the elliptic condition is satisfied, that is,  $\eta_\kappa = 1$ . Thin solid (broken) lines are for cases with  $\eta_\kappa < 1$  ( $> 1$ ).  $\eta_\kappa$  varies from 0.60 to 1.40 with an interval of 0.2. Note the opposite effect of  $\eta_\kappa$  on phase velocities of  $qP$  and  $qSV$ . (This figure is the same as fig. 3b of Kawakatsu, 2016a but in color.) The color version of this figure is available only in the electronic edition.

$$\sigma = \frac{\alpha_V^2}{\beta_V^2} (\varepsilon - \delta) = \frac{1}{2} \left( 1 - \eta_\kappa^2 \right) \left( \frac{A}{L} - 1 \right) \approx (1 - \eta_\kappa^2) \approx -2(\eta_\kappa - 1) \quad (\text{if } A \approx 3L), \quad (11)$$

in which  $\sigma$  follows the definition of Tsvankin and Thomsen (1994) (Kawakatsu, 2018) and is not Poisson's ratio. Therefore, the effect of this bias roughly scales with one-third of  $(\eta_\kappa - 1)$  if a Poisson solid-type character is assumed. If  $\eta_\kappa$  lies between 0.9 and 1.1, as seen in later examples, the  $V_P/V_S$  ratio bias will be less than  $\sim \pm 3.5\%$  and might not be so significant except for some peculiar situations, such as laminated melt layering (Fig. 4b) or shape-preferred orientation (SPO) of volatile-filled high aspect ratio cracks under shear.

It may be informative to compare equation (10) with ratios of  $V_P(45)$  to  $V_P(0)$  and  $V_{SV}(45)$  to  $V_{SV}(0)$  (numbers in parentheses denote incidence angles measured from the symmetry axis) (e.g., Okaya and Christensen, 2002) that measure the strength of the  $4\theta$  term of anisotropy. Assuming the absence of  $P$  anisotropy (i.e.,  $A = C$  and  $\varphi^{-1} = 1$ ), it can be shown that

$$\frac{\hat{V}_P(45)}{\hat{V}_P(0)} = \left[ 1 + \frac{1 - L/C}{2} (\eta_\kappa - 1) \right]^{1/2} \approx 1 + \frac{1}{6} (\eta_\kappa - 1), \quad (12)$$

and

$$\frac{\hat{V}_{SV}(45)}{\hat{V}_{SV}(0)} = \left[ 1 + \frac{1 - C/L}{2} (\eta_\kappa - 1) \right]^{1/2} \approx 1 - \frac{1}{2} (\eta_\kappa - 1), \quad (13)$$

in which  $\hat{\phantom{x}}$  denotes the absence of  $P$  anisotropy.

## DISCUSSION

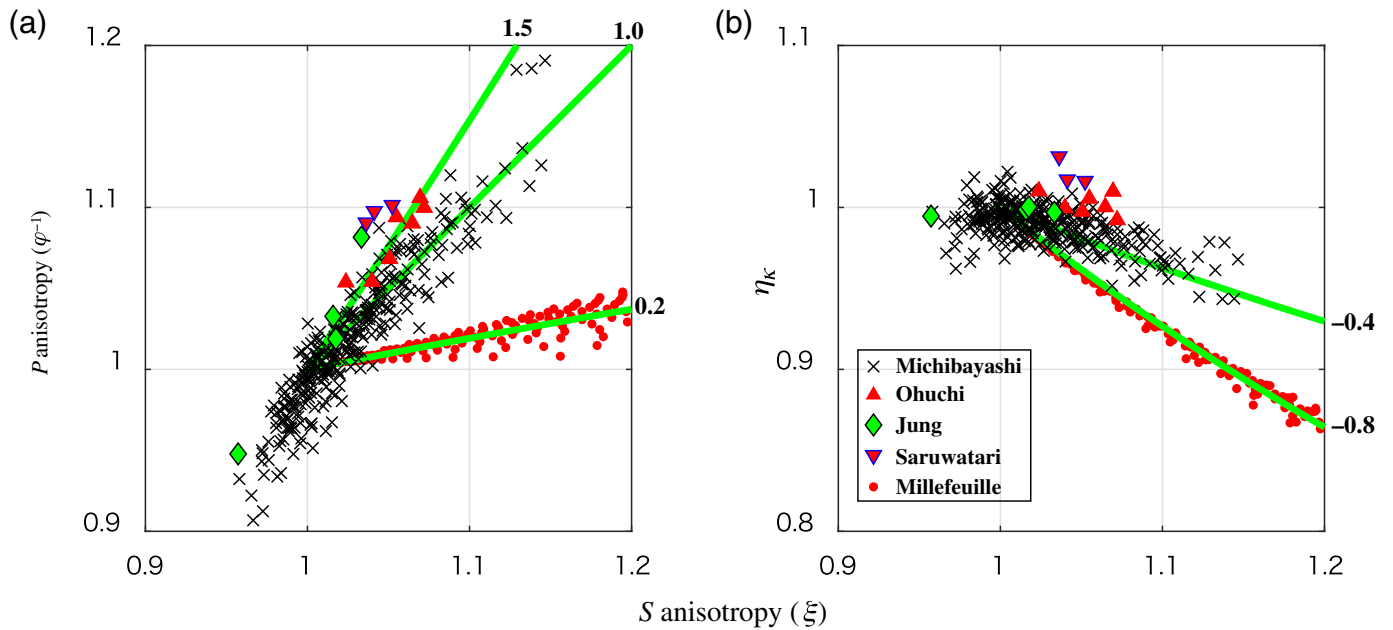
### Scaling among VTI parameters

**Mantle.** To find out to what extent the discussed consequences of VTI impact actual geophysical interpretation, understanding of the scaling among VTI parameters might be useful. Here, we compare two end-member scenarios for the mantle: olivine crystal-preferred orientation (CPO) fabrics and the laminated melt structure (millefeuille [MF] model). For the former, we assume that the crystallographic  $b$  axis is aligned in the vertical direction and its azimuthal (Montagner) average (Montagner and Nataf, 1986; Chen and Tromp, 2007) is considered for various fabrics (Saruwatari *et al.*, 2001; Jung *et al.*, 2006; Ohuchi *et al.*, 2011; Michibayashi *et al.*, 2016). For the latter, we employ a layered melt parameterization of Backus averaging (Backus, 1962) of a stack of two kinds of homogeneous isotropic layers: soft layers embedded in a background solid matrix (e.g., Kawakatsu *et al.*, 2009). We parameterize (1) the proportional reduction of rigidity of soft layers to the background by  $a$  ( $0 \leq a \leq 1$ ), (2) the proportional reduction of the bulk modulus by  $a/2$ , and (3) the volume fraction of soft layers by  $f$  ( $0 \leq f \leq 1$ ). Figure 4 shows the correlation among VTI parameters for such models. In the case of reported CPO fabrics (both natural and laboratory), there exists a strong positive scaling between  $S$ - and  $P$ -wave anisotropy, whereas for the MF model  $S$  anisotropy dominates:

$$\varphi^{-1} \sim \xi^{1.0-1.5} \quad (\text{for olivine}),$$

$$\varphi^{-1} \sim \xi^{0.2} \quad (\text{for MF}).$$

These two end-member models represent very different behaviors for receiver functions. For the MF model, as the dependence on  $P$  anisotropy is weak, the  $S$  wavespeed effect dominates the receiver functions. On the other hand, for the olivine case, as we discussed earlier, the  $P$ -anisotropy effect dominates. Because the scaling index ranges roughly from 1 to 1.5, the discussed dominance of  $P$  anisotropy could be even more significant than previously considered. In Figure 5a, we show synthetic waveforms, as in Figure 1, for some of the representative fabric models (A-, B-, C-, and E-type olivines of Jung *et al.*, 2006) for the lower anisotropic half-space; we set the reference velocities ( $\alpha_0, \beta_0$ ) of the lower layer equal to that of the surface layer. Then, we use anisotropy parameters of the models to construct the equivalent anisotropy lower



layer (Table 1). For example, a case of A-type olivine of Jung *et al.* (2006), which has strong  $P$  anisotropy ( $a_p = -3.9\%$ ) and mild  $S$  anisotropy ( $a_s = -1.6\%$ ) for azimuthally averaged VTI, shows a positive primary phase, whereas the C-type olivine ( $a_p = +2.7\%$ ,  $a_s = +2.2\%$ ) case shows a negative one. Compared with the case of 5%  $S$  velocity decreases, these particular olivine fabrics affect the  $P_s$ -phase amplitude by about half or less. For the MF model, model parameters of  $a = 0.92$  and  $f = 0.01$  give  $a_p = -0.6\%$ ,  $a_s = -5.0\%$ , and  $\eta_\kappa = 0.92$ . The absolute amplitude of the primary  $P_s$  phase is as large as that of the  $\Delta\beta_V = -5\%$  case, but half of the contribution comes from the  $\eta_\kappa$  effect (see fig. 2b of Kawakatsu, 2018). In reality, two end-member models may coexist, and other isotropic effects, such as temperature, may take roles that further complicate the interpretation. In addition, VTI could be just an azimuthal average of more general anisotropy. Therefore, for environments where seismic anisotropy is important, the interpretation of receiver functions may require careful attention.

It may be of interest to comment on the scaling between  $S$  (or  $P$ ) anisotropy and the fifth parameter,  $\eta_\kappa$ . For the MF case, a clear scaling,

**Figure 4.** Correlation among the anisotropy parameters for different fabric models for some representative ones: (a)  $S$  anisotropy ( $\xi$ ) versus  $P$  anisotropy ( $\varphi^{-1}$ ). (b)  $S$  anisotropy versus the fifth parameter ( $\eta_\kappa$ ). Symbols represent fabrics of natural mantle rocks (Michibayashi *et al.*, 2016) (cross); mantle xenolith (Saruwatari *et al.*, 2001) (reverse triangle); laboratory rocks (Ohuchi *et al.*, 2011, 2015) (triangle); Jung *et al.*, 2006) (diamond); and the millefeuille (MF) model (small solid circle). Thick lines are inferred scalings with various scaling indexes indicated by italicized numbers. The color version of this figure is available only in the electronic edition.

$$\eta_\kappa \sim \xi^{-0.8},$$

emerges, resulting in  $\eta_\kappa < 1$ . Although the natural olivine samples representing the lithospheric mantle (Michibayashi *et al.*, 2016) show scaling  $\eta_\kappa \sim \xi^{-0.4}$ , other fabrics show more scattered behavior. Notably, some mantle xenoliths exhibit  $\eta_\kappa \sim 1.03$ , comparable to the value suggested for the oceanic asthenosphere by Song and Kawakatsu (2012, 2013) to explain the trench-parallel fast direction of the subslab anisotropy (Long and Silver, 2008) as a simple consequence of the geometrical effect of tilted TI (TTI) at subduction zones.

TABLE 1  
VTI Parameters for Anisotropy Models in Figure 5

Model Name	$\varphi^{-1}$	$\xi$	$\eta_\kappa$	$a_p$ (%)	$a_s$ (%)
Millefeuille	1.013	1.105	0.917	-0.6	-5.0
A type	1.082	1.033	0.997	-3.9	-1.6
B type	1.033	1.016	0.999	-1.6	-0.8
C type	0.948	0.957	0.995	2.7	2.2
E type	1.019	1.017	1.000	-0.9	-0.9

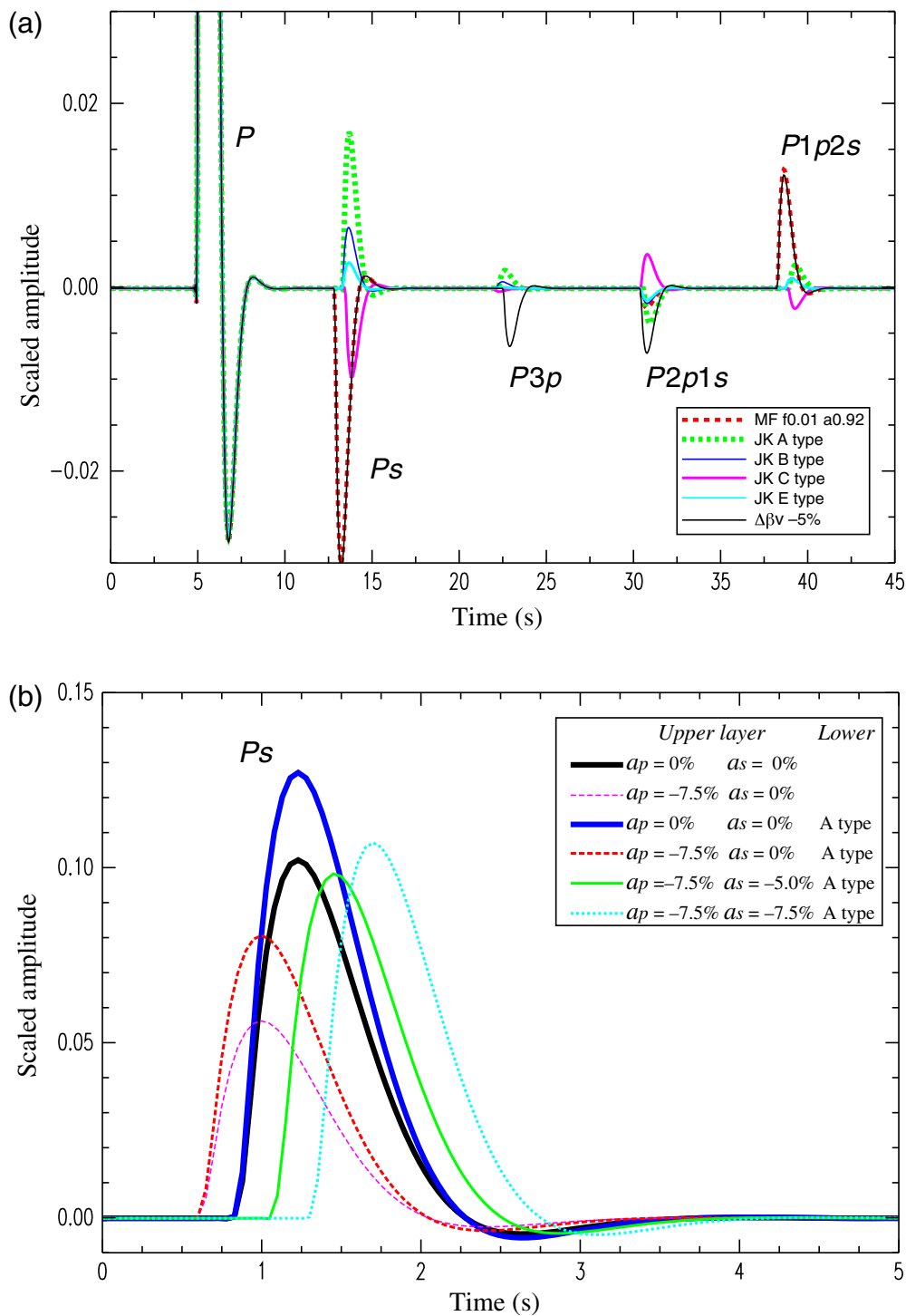


**Figure 5.** (a) Same as in Figure 1a (the radial component of a plane  $P$ -wave incidence), but for various fabric models. JK stands for Jung *et al.* (2006) fabrics (A, B, C, and E types). See the [Scaling Among VTI Parameters](#) section for more details. (b) Examples of radial-component  $P_s$  phases in realistic Moho cases. The background model is the same as in Figure 1a, but  $S$  velocity increases by 15% at the interface to simulate the Moho situation. Different lines indicate  $P_s$  phases for corresponding cases shown in the legend: (thick dark solid) both layers isotropic, (thin broken) upper layer radially anisotropic only in  $P$  wave, lower layer isotropic, (thick medium solid; thinner broken, solid, and dotted lines) upper layer radially anisotropic as indicated in legend, lower layer radially anisotropic with that of the olivine A-type fabric (Table 1). Time 0 s corresponds to 7 s after the incident  $P$  wave. The color version of this figure is available only in the electronic edition.

**Crust.** Figure 6 presents the correlation among the VTI parameters for the crustal fabrics reported by Brownlee *et al.* (2017). Considering the possibility of complex fabrics orientation in a crust setting, here we construct a series of VTI models for each fabric given by azimuthal averaging (Montagner and Nataf, 1986) of an arbitrarily rotated elastic tensor (the rotation is done with a  $30^\circ$  interval for each Euler angle that results in 72 [ $12 \times 6$ ; rotation around the original  $z$ -axis can be azimuthally averaged out] VTI models for each original fabric). Among the various rock types classified in Brownlee *et al.* (2017), those fabrics grouped as “amphibolite” indicate clear correlations of the VTI parameters (Fig. 6a); the trend is generally similar to that for the mantle fabrics shown in Figure 4, but with stronger anisotropy (1.5 ~ 2 times), and thus a similar qualitative argument for the impact of the VTI on the receiver functions can be made. As for the remaining fabrics, points are more scattered, but still somewhat similar correlations appear to emerge (the supplemental material). Those consisting of a significant mica component ( $>10\%$ ) can have very strong anisotropy ( $\xi$  or  $\varphi^{-1}$  up to 1.8; Figs. S2 and S4, available in the supplemental material). Considering that the  $S$ -velocity increase at Moho is  $\sim 15\%$ ,  $a_p \sim \pm 15\%$  (i.e.,  $\varphi^{-1} \sim 1.0 \mp 0.3$ ) could have comparable effect. Therefore, these fabrics could potentially impact the interpretation of receiver function signals from Moho.

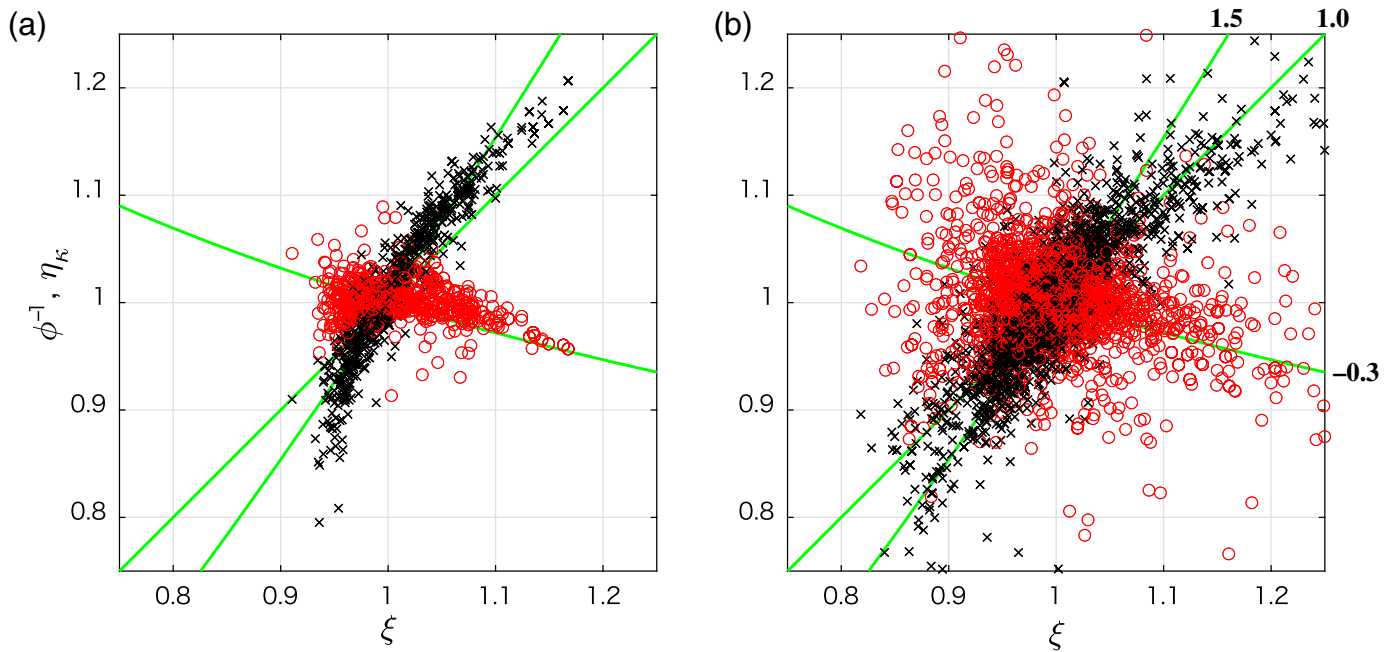


**Figure 6.** Correlation among the anisotropy parameters for crustal fabrics of [Brownlee et al. \(2017\)](#):  $S$  anisotropy ( $\xi$ ) versus  $P$  anisotropy ( $\phi^{-1}$ ) (cross) and  $S$  anisotropy versus the fifth parameter ( $\eta_{\kappa}$ ) (open circle). (a) Amphiolite and (b) the remaining fabrics. Solid lines are reference scalings with various indexes indicated by italicized numbers. Compare Figures S1–S10 for more detail. The color version of this figure is available only in the electronic edition.

To model a more realistic Moho structure, we simulate radial component seismograms for a  $P$ -wave incidence into an interface at a depth of 80 km with a  $\sim 15\%$   $S$ -velocity increase (Fig. 5b). The thick dark solid line represents a reference case in which both layers are isotropic: the amplitude of  $P_s$  phase is  $\sim 10\%$  of that of the direct  $P$  wave. When we introduce  $P$  anisotropy of  $a_p = -7.5\%$  ( $\phi^{-1} \sim 1.15$ ) in the upper-crustal layer, the  $P_s$  amplitude is reduced by about half as expected from the previous argument (thin broken line). Instead, if we introduce radial anisotropy equivalent of A-type olivine (generally believed to be the most dominant fabric in the mantle; Table 1) in the lower layer, the  $P_s$  amplitude increases by about 30% (thick medium line). We compare this with three additional cases in which the upper layer has  $P$  anisotropy of  $a_p = -7.5\%$  and  $S$  anisotropy of  $a_s = 0\%, -5\%, -7.5\%$ , respectively, representing a pure  $P$ -anisotropy case and two different scalings of  $\phi^{-1} \sim \xi^{1.5}$  and  $\phi^{-1} \sim \xi^{1.0}$ . Here, the reduction of the  $P_s$  amplitude ranges from  $\sim 40\%$  to  $\sim 15\%$ , and the decrease of the reduction is due to the competing effect of the  $P$  and  $S$  anisotropy. The range of the  $P_s$ -amplitude variation exemplified here is larger than the uncertainty of the  $S$ -wave velocity jump at the continental Moho estimated from the array stacked receiver functions (e.g., [Niu and James, 2002](#)). Therefore, crustal  $P$  anisotropy discussed here should have observable effects on  $P$ -wave receiver functions. As for other discontinuities with smaller velocity changes, such as LAB or MLD, the relative significance of  $P$  anisotropy could be more severe depending on the actual situation.

In summary, the situation for both mantle and crust could be very complicated, and invoking a probabilistic parameter space search (e.g., [Mosegaard and Tarantola, 1995](#); [Bodin et al., 2012](#)) with appropriate a priori constraints might help to infer the actual structure. It should be also noted that variations of slowness and azimuth of conversion amplitudes in receiver

functions may allow distinctions between isotropic  $S$  contrasts and anisotropic  $P$  contrasts.

### Intrinsic versus extrinsic VTI

VTI or radial anisotropy discussed in this article represents, by definition, a hexagonally anisotropic system with the symmetry axis that is vertical. Such a system can be considered a realization of nature in two ways: intrinsic and extrinsic VTI. Intrinsic VTI occurs when the symmetry axes of hexagonal symmetry crystals are aligned vertically or when the horizontally laminated structure dominates (e.g., MF). Extrinsic VTI occurs in other cases as a result of azimuthal averaging of arbitrary anisotropy. In the case of intrinsic VTI, discussions presented in this article can be taken as they are. In the case of extrinsic VTI, the azimuthal variation of receiver functions or dispersion measurements has to be considered, and in the data analysis, azimuthal averaging is essential. This is a common practice for Rayleigh-wave dispersion analysis. On the other hand, for receiver function analysis, how (back-)azimuthal averaging of receiver functions of arbitrary anisotropy compares with that of azimuthally averaged VTI might not be straightforward (e.g., [Levin and Park, 1998](#)) when the azimuthal anisotropy term is strong compared with the radial anisotropy one; this may deserve careful attention but is

beyond the scope of this article. It should be noted that, in the recent analyses, strong radial anisotropy is reported in the oceanic crust and mantle (Nettles and Dziewonski, 2008; Russell *et al.*, 2019) and beneath active volcanos (Jaxybulatov *et al.*, 2014; Nagaoka, 2020). It is also worth mentioning that Levin and Park (1998) reported the importance of  $P$  anisotropy in the generation of  $P$ -to- $S$  converted  $P$  coda waves, although anisotropy in their analysis refers to that of tilted transverse isotropy.

## CONCLUSION

We discussed several nontrivial consequences of wave propagation in a transverse isotropy system and presented example cases to show the significant effect of  $P$ -wave anisotropy on both receiver function analysis and Rayleigh-wave dispersion analysis. This suggests that, in the presence of anisotropy, careful interpretation of receiver functions and ambient-noise Rayleigh-wave dispersion is required. We also presented scalings among VTI parameters of the crust and mantle materials or models that might help with delineating to what extent this effect becomes important and can be used in the actual problems as a priori constraints.

## DATA AND RESOURCES

No seismic data were used in this article. The supplemental material presents correlations among the VTI parameters for each of the crustal fabrics reported by Brownlee *et al.* (2017).

## ACKNOWLEDGMENTS

This research is partly supported by Japan Society for the Promotion of Science (JSPS) KAKENHI Grant Numbers 17H02948, 18H03735, and 19K21892. The author thanks Katsuyoshi Michibayashi and Sarah Brownlee for the natural fabric data of Michibayashi *et al.* (2016) and Brownlee *et al.* (2017) and Alex Song for discussions. The author also thanks two reviewers and the associate editor for comments that significantly improved this article and, particularly, Joshua Russell for thoughtful comments and questions.

## REFERENCES

Abt, D. L., K. M. Fischer, S. W. French, H. A. Ford, H. Yuan, and B. Romanowicz (2010). North American lithospheric discontinuity structure imaged by  $P_s$  and  $S_p$  receiver functions, *J. Geophys. Res.* **115**, no. B09301, doi: [10.1029/2009JB006914](https://doi.org/10.1029/2009JB006914).

Aki, K., and P. Richards (1980). *Quantitative Seismology: Theory and Methods*, W. H. Freeman, New York, New York.

Ammon, C. J. (1991). The isolation of receiver effects from teleseismic  $P$  waveforms, *Bull. Seismol. Soc. Am.* **81**, 2504–2510.

Anderson, D. L., and A. M. Dziewonski (1982). Upper mantle anisotropy: Evidence from free oscillations, *Geophys. J. Int.* **69**, 383–404.

Backus, G. E. (1962). Long-wave elastic anisotropy produced by horizontal layering, *J. Geophys. Res.* **67**, 4427–4440.

Becker, T., S. Chevrot, V. Schulte-Pelkum, and D. K. Blackman (2006). Statistical properties of seismic anisotropy predicted by upper mantle geodynamic models, *J. Geophys. Res.* **111**, no. B08309, doi: [10.1029/2005JB004095](https://doi.org/10.1029/2005JB004095).

Bodin, T., M. Sambridge, H. Tkalcic, P. Arroucau, K. Gallagher, and N. Rawlinson (2012). Transdimensional inversion of receiver functions and surface wave dispersion, *J. Geophys. Res.* **117**, no. B02301, doi: [10.1029/2011JB008560](https://doi.org/10.1029/2011JB008560).

Brenguier, F., M. Campillo, C. Hadziioannou, N. M. Shapiro, R. M. Nadeau, and E. Larose (2008). Postseismic relaxation along the San Andreas fault at Parkfield from continuous seismological observations, *Science* **321**, 1478–1481.

Brenguier, F., N. M. Shapiro, M. Campillo, V. Ferrazzini, Z. Duputel, O. Coutant, and A. Nercessian (2008). Towards forecasting volcanic eruptions using seismic noise, *Nature Geosci.* **1**, 126–130.

Brownlee, S. J., V. Schulte-Pelkum, A. Raju, K. Mahan, C. Condit, and O. F. Orlandini (2017). Characteristics of deep crustal seismic anisotropy from a compilation of rock elasticity tensors and their expression in receiver functions, *Tectonics* **36**, 1835–1857.

Chen, M., and J. Tromp (2007). Theoretical and numerical investigations of global and regional seismic wave propagation in weakly anisotropic earth models, *Geophys. J. Int.* **168**, 1130–1152.

Crampin, S. (1984). Effective anisotropic elastic constants for wave propagation through cracked solids, *Geophys. J. Roy. Astron. Soc.* **76**, 135–145.

Dziewonski, A. M., and D. L. Anderson (1981). Preliminary reference Earth model, *Phys. Earth Planet. In.* **25**, 297–356.

Jaxybulatov, K., N. M. Shapiro, I. Koulakov, A. Mordret, M. Landes, and C. Sens-Schonfelder (2014). A large magmatic sill complex beneath the Toba caldera, *Science* **346**, 617–619.

Jung, H., I. Katayama, Z. Jian, T. Hiraga, and S. Karato (2006). Effect of water and stress on the lattice-preferred orientation of olivine, *Tectonophysics* **421**, 1–22.

Kawakatsu, H. (2016a). A new fifth parameter for transverse isotropy, *Geophys. J. Int.* **204**, 682–685.

Kawakatsu, H. (2016b). A new fifth parameter for transverse isotropy II: Partial derivatives, *Geophys. J. Int.* **206**, 360–367.

Kawakatsu, H. (2018). A new fifth parameter for transverse isotropy III: Reflection and transmission coefficients, *Geophys. J. Int.* **213**, 426–433.

Kawakatsu, H., P. Kumar, Y. Takei, M. Shinohara, T. Kanazawa, E. Araki, and K. Suyehiro (2009). Seismic evidence for sharp lithosphere–asthenosphere boundaries of oceanic plates, *Science* **324**, 499–502.

Kawakatsu, H., J.-P. Montagner, and T.-R. A. Song (2015). On DLA's  $\eta$ , in *The Interdisciplinary Earth: A Volume in Honor of Don L. Anderson*, GSA and AGU, 33–38.

Levin, V., and J. Park (1998).  $P$ - $SH$  conversions in layered media with hexagonally symmetric anisotropy: A Cookbook, *Pure Appl. Geophys.* **151**, 669–697.

Lin, F.-C., M. H. Ritzwoller, Y. Yang, M. P. Moschetti, and M. J. Fouch (2010). Complex and variable crustal and uppermost mantle seismic anisotropy in the western United States, *Nature Geosci.* **4**, 55–61.

Long, M., and P. G. Silver (2008). The subduction zone flow field from seismic anisotropy: A global view, *Science* **319**, 315–318.

Michibayashi, K., D. Mainprice, A. Fujii, S. Uehara, Y. Shinkai, Y. Kondo, Y. Ohara, T. Ishii, P. Fryer, S. H. Bloomer, *et al.* (2016). Natural olivine crystal-fabrics in the western Pacific convergence region: A new method to identify fabric type, *Earth Planet. Sci. Lett.* **443**, 70–80.

- Montagner, J.-P., and D. L. Anderson (1989). Constraints on elastic combinations inferred from petrological models, *Phys. Earth Planet. In.* **54**, 82–105.
- Montagner, J.-P., and H.-C. Nataf (1986). On the inversion of the azimuthal anisotropy of surface waves, *J. Geophys. Res.* **91**, 511–520.
- Mosegaard, K., and A. Tarantola (1995). Monte Carlo sampling of solutions to inverse problems, *J. Geophys. Res.* **100**, 12–431.
- Nagaoka, Y. (2020). Study on seismic velocity structure beneath active volcanoes by seismic interferometry, *Ph.D. Thesis*, The university of Tokyo.
- Nettles, M., and A. M. Dziewonski (2008). Radially anisotropic shear velocity structure of the upper mantle globally and beneath North America, *J. Geophys. Res.* **113**, no. B02303, doi: [10.1029/2006JB004819](https://doi.org/10.1029/2006JB004819).
- Nishida, K., H. Kawakatsu, and K. Obara (2008). Three-dimensional crustal S wave velocity structure in Japan using microseismic data recorded by Hi-net tiltmeters, *J. Geophys. Res.* **113**, no. B10302, doi: [10.1029/2007JB005395](https://doi.org/10.1029/2007JB005395).
- Nishida, K., Y. Mizutani, M. Ichihara, and Y. Aoki (2020). Time-lapse monitoring of seismic velocity associated with 2011 Shinmoe-dake eruption using seismic interferometry: An extended Kalman filter approach, *J. Geophys. Res.* **125**, e2020JB020180.
- Niu, F., and D. E. James (2002). Fine structure of the lowermost crust beneath the Kaapvaal craton and its implications for crustal formation and evolution, *Earth Planet. Sci. Lett.* **200**, 121–130.
- Ohuchi, T., T. Kawazoe, Y. Nishihara, N. Nishiyama, and T. Irifune (2011). High pressure and temperature fabric transitions in olivine and variations in upper mantle seismic anisotropy, *Earth Planet. Sci. Lett.* **304**, 55–63.
- Ohuchi, T., Y. Nishihara, Y. Seto, T. Kawazoe, M. Nishi, G. Maruyama, M. Hashimoto, Y. Higo, K. I. Funakoshi, A. Suzuki, *et al.* (2015). In situ observation of crystallographic preferred orientation of deforming olivine at high pressure and high temperature, *Phys. Earth Planet. In.* **243**, 1–21.
- Okaya, D. A., and N. I. Christensen (2002). Anisotropic effects of non-axial seismic wave propagation in foliated crustal rocks, *Geophys. Res. Lett.* **29**, 2-1–2-4.
- Russell, J. B., J. B. Gaherty, P.-Y. P. Lin, D. Lizarralde, J. A. Collins, G. Hirth, and R. L. Evans (2019). High-resolution constraints on Pacific upper mantle petrofabric inferred from surface-wave anisotropy, *J. Geophys. Res.* **124**, 631–657.
- Saruwatari, K., S. Ji, C. Long, and M. H. Salisbury (2001). Seismic anisotropy of mantle xenoliths and constraints on upper mantle structure beneath the southern Canadian Cordillera, *Tectonophysics* **339**, 403–426.
- Shapiro, N. M., and M. Campillo (2004). Emergence of broadband Rayleigh waves from correlations of the ambient seismic noise, *Geophys. Res. Lett.* **31**, L07614, doi: [10.1029/2004GL019491](https://doi.org/10.1029/2004GL019491).
- Song, T.-R. A., and H. Kawakatsu (2012). Subduction of oceanic asthenosphere: Evidence from sub-slab seismic anisotropy, *Geophys. Res. Lett.* **39**, L17301, doi: [10.1029/2012GL052639](https://doi.org/10.1029/2012GL052639).
- Song, T.-R. A., and H. Kawakatsu (2013). Subduction of oceanic asthenosphere: A critical appraisal in central Alaska, *Earth Planet. Sci. Lett.* **367**, 82–94.
- Takeuchi, H., and M. Saito (1972). Seismic surface waves, in *Seismology: Surface Waves and Earth Oscillations, Methods in Computational Physics*, Vol. 11, Academic Press, New York, New York, 217–295.
- Thomsen, L. (1986). Weak elastic anisotropy, *Geophysics* **51**, 1954–1966.
- Tsvankin, I., and L. Thomsen (1994). Nonhyperbolic reflection move-out in anisotropic media, *Geophysics* **59**, 1290–1304.

---

Manuscript received 11 June 2020  
Published online 10 November 2020